Role of edge effects and fluid depth in azimuthal Faraday waves

P. Wilson,[1] X. Shao,[2] J. R. Saylor,[1] and J. B. Bostwick[1,*]
[1]Department of Mechanical Engineering, Clemson University, Clemson, South Carolina 29634, USA
[2]Department of Chemical and Biomolecular Engineering, Johns Hopkins University, Baltimore, Maryland 21218, USA

(Received 19 May 2021; accepted 4 January 2022; published 24 January 2022)

Faraday waves are created in experiment by mechanically vibrating a cylindrical container. Frequency scans are performed, and the acceleration threshold above which a surface wave appears is measured using a laser light approach, giving the instability tongue in frequency-acceleration space. The spatial structure of the surface wave, which conforms to the cylindrical container for wavelengths comparable to the container size, is determined using long-exposure-time white light imaging and is defined by the mode number pair (n, ℓ). Edge conditions at the container sidewall are controlled to create a (i) pinned or (ii) freely sliding contact-line. The driving frequency with the smallest threshold acceleration is identified as the natural frequency for that particular mode number pair. A theoretical model is developed using a viscous potential approximation to compute the natural oscillations of a viscoelastic material in a cylindrical container with a flat interface for both a pinned and a freely sliding contact-line. A closed-form expression is given for the freely sliding case, and a Rayleigh-Ritz procedure is used for the pinned case. The agreement is good between theoretical predictions and experimental observations for Triton/water mixtures, glycerol/water mixtures, and agarose gels, notwithstanding the large range in parameter space and the very different boundary conditions considered.

DOI: 10.1103/PhysRevFluids.7.014803

I. INTRODUCTION

Faraday waves have been a paradigm for pattern formation on liquid/gas interfaces since their discovery in 1831 [1]. Since that time, a large volume of literature has been produced due to a sustained interest in both the physics and mathematics of Faraday waves [2,3], but also for their many applications, such as spray cooling, drop atomization [4–6], particle redistribution [7,8], turbulent mixing [9], and as a model for capillary wave gas transport [10–12]. More recently, sustained interest in cell printing for tissue engineering has led to the patterning of material/gas interfaces with cells in order to facilitate the growth of tissue scaffolds [13,14]. Here bioinks, such as agarose or alginate gel, are used as the working material [15,16]. The above applications rely upon a fundamental understanding of the spatial and temporal structure associated with Faraday waves, and this largely depends upon the material properties, fluid thickness, and edge (wetting) conditions between the interface and container. In this paper, we explore these factors in a combined experimental/theoretical study of Faraday wave formation in a cylindrical container, categorizing the effect of (i) the edge effects and (ii) the fluid depth for viscoelastic materials.

Faraday waves are generated in a typical experiment by vertically vibrating a fluid-filled container [17–19]. The resulting surface wave exhibits a subharmonic response, oscillating at half the driving frequency, consistent with the parametric oscillations described by the Mathieu equation,

*jbostwi@clemson.edu

provided the experimental conditions lie within the "instability tongue" in the driving frequency-acceleration amplitude space [20]. Of particular note for our study is the frequency with minimum threshold acceleration at the bottom of the tongue, which can be identified as the natural frequency for that particular mode shape. We note that there also exist harmonic and superharmonic instability tongues to the Mathieu equation, but these generally have larger threshold accelerations than the fundamental subharmonic tongue. However, there are exceptions, such as the case of a thin viscous fluid layer where the harmonic instability tongue has lower onset acceleration than the subharmonic one, conditions far different from the ones considered here [21,22].

The majority of research on Faraday waves has focused on Newtonian fluids, though important work has been conducted on the viscoelastic case [23–26]. In this more complicated viscoelastic case, the complex modulus $G' + iG''$ must be considered, where the storage modulus (elasticity) G' and the loss modulus (viscosity) G'' are often frequency-dependent [27]. Our interest is in contrasting viscous and elastic effects, and for this reason we use (i) glycerol/water mixtures and (ii) agarose gels to investigate the role of viscosity and elasticity, respectively. Glycerol/water mixtures provide a range of viscosity μ at essentially zero elasticity, while agarose gels provide a range of shear modulus G with relatively small viscosity, and both have material properties that are constant over the range of experimental driving frequencies. For surface tension driven phenomena, two dimensionless numbers define the viscoelastic properties: the Ohnesorge number $\mathrm{Oh} \equiv \mu/\sqrt{\rho R\sigma}$ and the elastocapillary number $\mathrm{Ec} \equiv GR/\sigma$ [28,29].

The surface wave structure conforms to the container geometry whenever the wavelength is comparable to the container size. For a cylindrical container, these are Bessel functions defined by the mode number pair (n, ℓ) [30–32]. The edge conditions at the container sidewall play an important role in Faraday wave onset. Here we investigate (i) pinned contact-line conditions created by filling the container to the brim such that the contact-line is immobilized by the sharp container edge [31], and (ii) free sliding conditions using a high concentration solution of a soluble surfactant in a nonbrimful situation [32,33]. We note that free sliding conditions can also be fabricated by two or more carefully chosen immiscible liquids, but that is not our interest [34,35]. Lastly, we note that the presence of a meniscus at the container sidewall can induce harmonic edge waves whenever the contact-angle $\alpha \neq 90^\circ$, and we pay particular attention to create a perfectly flat interface to avoid such motions [36].

In parallel with our experimental investigation, we develop a theoretical model for surface waves in a cylindrical container filled with a viscoelastic material and either (i) a pinned or (ii) a freely sliding contact-line. With regard to the latter, we derive a closed-form expression for the dispersion relationship as it depends upon Oh, Ec, the Bond number Bo, and the liquid aspect ratio h. The analysis for the pinned condition is not as straightforward, as this condition is incompatible with the no-penetration condition on the container sidewall. Our approach is to formulate the governing equation using linear operators, and to apply the variational approach of Rayleigh-Ritz over a constrained function space. This specific technique has been applied to constrained drops [37] and rivulets [38]. Other researchers have addressed this problem via Lagrange multipliers [39,40] and singular pressure (contact-force) at the contact-line [41]. Note that we ignore any dynamic wetting effects that give rise to contact-line or Davis dissipation [42–45]. Our theoretical predictions compare favorably with our large experimental data set over a range of experimental parameters.

II. EXPERIMENT

Surface waves were excited using the experimental setup shown in Fig. 1, wherein a circular plexiglass tank of radius $R = 35$ mm was affixed to a Labworks ET-139 electromechanical shaker. Although two fluid heights were considered in this work, three tanks were used, with heights of $H =$ 7, 22, and 27 mm. The 7- and 22-mm-high tanks were used for the pinned boundary condition cases using a procedure described below. To implement the sliding boundary condition cases, the 22 mm tank was used for the 7 mm fluid thickness case, the 7-mm-deep tank being unsuitable since the sliding meniscus of a 7-mm-thick fluid layer would spill over the wall. Similarly, for the 22 mm fluid

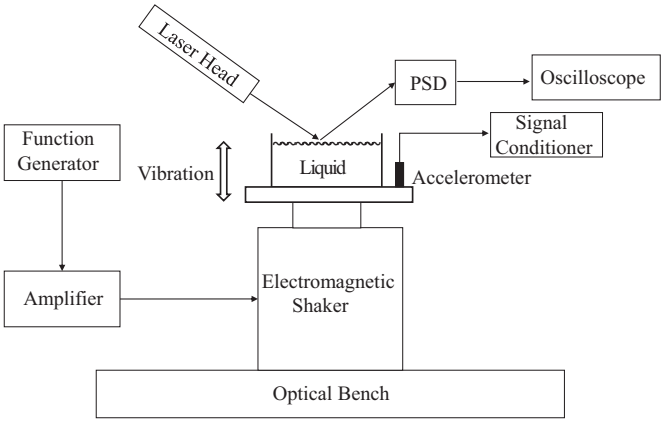

FIG. 1. Experimental schematic, reproduced with permission from Shao *et al.* [46].

thickness case, the 27-mm-deep tank was used for the sliding boundary condition case. The shaker was driven by an Agilent 33220A function generator and Labworks PA-141 amplifier combination providing vertical motion of the tank over a range of driving frequencies f_d and accelerations a measured with a PCB 352C33 accelerometer and a PCB 482C05 signal conditioner combination. The average min-max of the acceleration signal defines the acceleration amplitude A, which we used to characterize the driving force.

To enable the tuning of material properties, glycerol/water mixtures were used. Pure glycerol was mixed with doubly distilled water using the volume ratios given in Table I where the material properties are presented: μ the viscosity, ρ the density, and σ the surface tension [47]. Note that pure water was used as the limiting case mixture. These viscous mixtures can be defined by the dimensionless Ohnesorge number $\mathrm{Oh} \equiv \mu/\sqrt{\rho R \sigma}$. In recent work by Shao *et al.* [26], agarose hydrogels were used to investigate the role of elasticity in Faraday waves, and we will compare our theoretical model to those results in a forthcoming section. The relevant dimensionless parameter for gels is the elastocapillary number $\mathrm{Ec} \equiv GR/\sigma$, which describes the relative importance of elastic to surface tension forces. If we assume the surface tension for agarose gel is $\sigma = 72$ mN/m (a reasonable assumption given the low polymer concentrations used here), this gives a range of $\mathrm{Ec} = 0.131$–5.93. Viscoelastic materials are characterized by Oh and Ec.

Edge conditions on the container sidewall were prescribed so as to either (i) restrict (pinning) or (ii) allow (free sliding) contact-line motion, as illustrated in Fig. 2. For both edge conditions, we ensured that the liquid/gas interface was perfectly flat (i.e., with a contact angle of 90°) so as not to excite harmonic edge waves. Pinned conditions were attained by filling the tank to the brim such that the contact-line was pinned at the edge of the container, as shown in Fig. 2(b). At this point the tank was slightly overfilled, and the requisite amount of fluid was removed to ensure a flat surface. Our experiments with glycerol/water mixtures and agarose gels all had a pinned contact-line. To realize free-sliding conditions, the liquid does not completely fill the container [cf. Fig. 2(a)] and we added a soluble surfactant (Triton-X100) to doubly distilled water in a large enough concentration to

TABLE I. Liquid properties of water:glycerol mixtures, surface tension σ, viscosity μ, and density ρ.

water:glycerol	1:0	2:1	1:1	1:2
Surface tension (N/m)	71.6	69.1	66.1	65.3
Viscosity (mPa s)	0.96	3.0	6.8	20.6
Density (kg/m^3)	997	1093	1139	1182

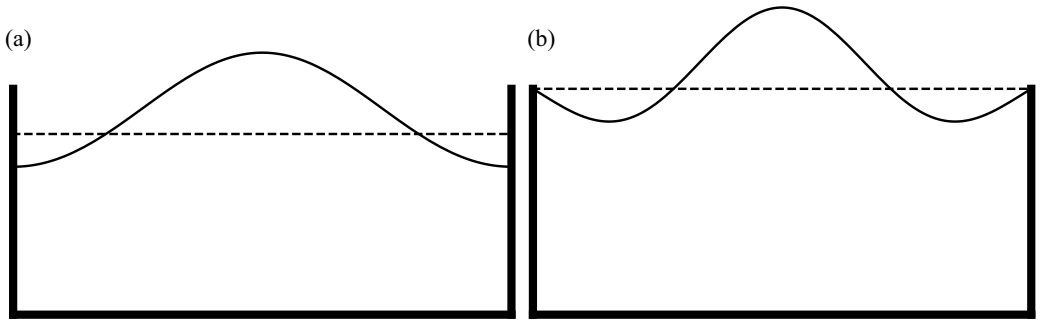

FIG. 2. Illustration of the experimental conditions for (a) a freely sliding and (b) a pinned contact-line.

allow for a mobile contact-line. This approach has been applied by Henderson and Miles [32]. For our experiments, we used a Triton-X100/water concentration of 0.0132 g/300 mL, which yields a surface tension $\sigma = 40.73$ mN/m, as measured by a Nanoscience Sigma 702 tensiometer. The range in surface tension attained by using doubly distilled water and the Triton/water solution yields a range in Bond number of $\mathrm{Bo} \equiv \rho g R^2/\sigma = 167$–$295$. Lastly, we note that surfactants typically have an inherent surface elasticity and surface viscosity, and these surface properties can affect the natural frequency and decay rate of the waves [48]. For the range of driving frequencies explored here, we estimate these surface properties to minimally affect the wave frequency, which is our interest here.

Faraday waves are defined by an instability tongue in the frequency-acceleration space. Frequency scans were performed using a 0.2 Hz interval, and we measured the onset acceleration using the laser light system shown in Fig. 1, whereby a helium-neon laser beam (632.8 nm wavelength) is incident on the free surface and reflected to a position sensitive detector (PSD). The output signal from the PSD is processed through a fast Fourier transform (FFT) operation on an oscilloscope, giving the surface wave frequency. For Faraday waves, the observed frequency f_o was half the driving frequency $f_o = 0.5 f_d$, and for a fixed driving frequency f_d, we approached the acceleration threshold by increasing the tank acceleration until we observed the rapid growth of a frequency peak with $f_o = 0.5 f_d$ on the oscilloscope. We recorded this acceleration A_u as the upper limit of the threshold acceleration for that driving frequency, and then we decreased the amplitude until the frequency peak disappeared. This defines the lower limit of the threshold acceleration A_l. We then performed several iterations where we changed the amplitude in 0.2 m/s^2 increments and waited for 15 s between each change, until the difference in $A = (A_u + A_l)/2$ between two iterations was less than 0.2 m/s^2, at which point we reported this average value A as the experimental threshold acceleration. We note that a complete acceleration scan was performed before moving the 0.2 Hz interval to the next frequency.

The spatial structure of the surface wave was determined using long exposure time (0.6 s) white light imaging. Here collimated light was produced by a lens located one focal length $f = 300$ mm from a white light source, which was incident at the liquid surface and reflected back to a digital camera (Canon EOS Rebel T3i) with a Canon EF-S 18-55 mm lens. Typical wave patterns are shown in Fig. 3. Here the regions where the wave slope is zero (i.e., the peak or trough) appear bright, whereas the regions where the wave slope is nonzero (i.e., the nodes) appear dark. Larger slopes lead to darker regions. Two-dimensional (2D) cross-correlations between the experimental wave pattern and the Bessel function $J_\ell(k_{n\ell} r)\cos(\ell\theta)$, defined in cylindrical coordinates (r, θ), were used to determine the spatial structure. Here ℓ is the azimuthal mode number and $k_{n\ell}$ is computed from the roots of $J'_\ell(k_{n\ell} R) = 0$ (n is the numerical order of those roots). Further details of this experimental approach can be found in Ref. [46]. Other methods for obtaining wave slope and for imaging waves are also available [49–52], though the approach used here was optimal for the goals of this study.

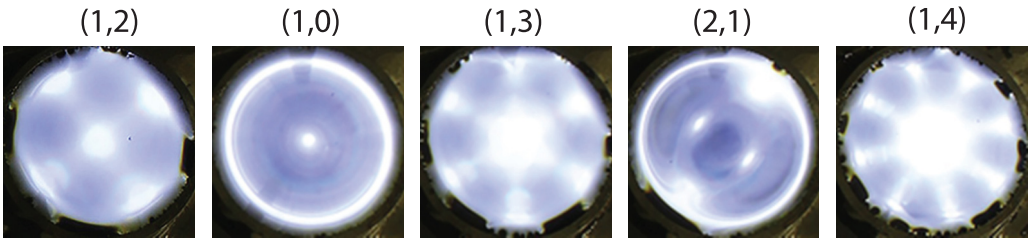

FIG. 3. Experimentally observed modes (n, ℓ).

III. EXPERIMENTAL RESULTS

Figure 4 shows the results of a typical frequency scan for water with a pinned contact-line condition. For a given driving frequency f_d the interface is flat below the threshold acceleration and exhibits an oscillating surface wave pattern above the threshold acceleration. Each surface wave mode (n, ℓ) has an associated instability tongue in the (f_d, A) space over which that mode is excited. The frequency associated with the minimum threshold acceleration is the natural frequency for that mode. The accelerations at which onset occurred were very repeatable. Indeed, we always obtained the same result at a given frequency. This does not mean that our method is perfect, only that the uncertainty in the onset of Faraday waves is smaller than the 0.2 m/s^2 acceleration increments used here. Regarding the frequency, the error is bounded by the interval size, which was 0.2 Hz in driving frequency or 0.1 Hz in natural frequency.

We compare the experimentally observed natural frequency with theoretical predictions in the next section. The ordering of modes with respect to increasing driving frequency for these experimental conditions is (1,2),(1,0),(1,3),(2,1),(1,4) with typical mode shapes shown in Fig. 3. This ordering does not change for the experiments reported here. We observed the (1,1) sloshing mode for even lower driving frequencies, but we were unable to resolve the instability tongue due to large amplitude motions that caused spilling of the liquid over the container edge.

Treating pure water as our base case, we now systematically investigate how (i) edge effects, (ii) liquid height, and (iii) viscosity affect the instability tongues.

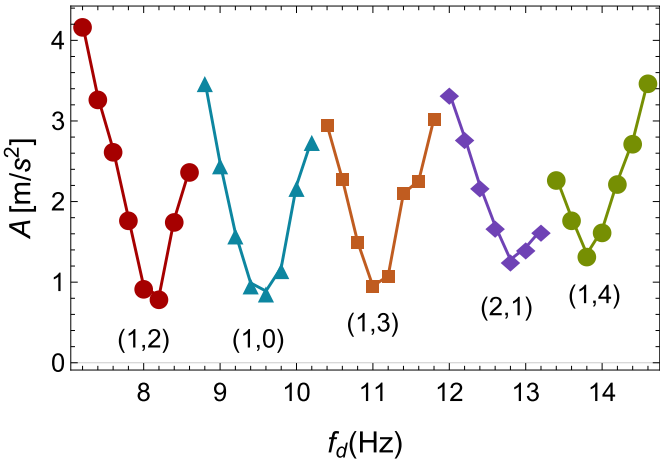

FIG. 4. Instability tongue for water with a pinned contact-line and $H = 7$ mm plotting acceleration A against driving frequency f_d.

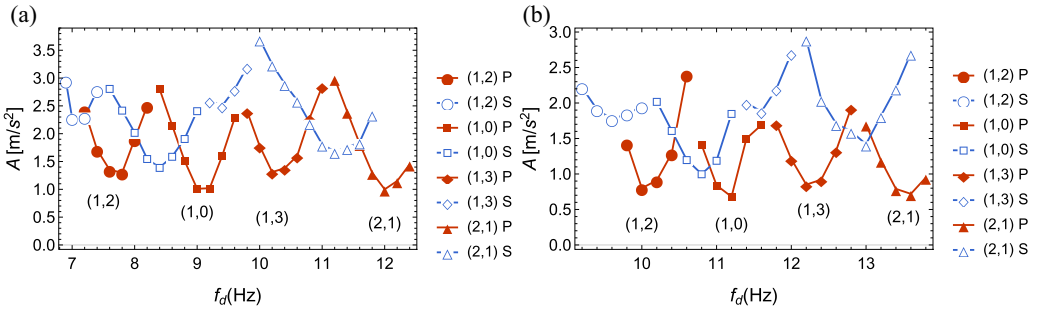

FIG. 5. Acceleration A against driving frequency f_d for the Triton/water mixture contrasting the free-sliding (S) and pinned (P) contact-line condition for fluid height (a) $H = 7$ mm and (b) $H = 22$ mm.

Figure 5 is a plot of the instability tongues for Triton/water mixtures contrasting the pinned (P) and free sliding (S) edge conditions and showing the effect of the fluid height H. Here we note that the threshold acceleration A for the pinned case is always smaller than that for the free sliding case, indicating that more inertia is required to excite modes with a mobile contact-line. This makes sense because of the energy dissipation due to sliding friction that must be overcome in the free sliding case that is not present for the pinned case. The natural frequencies for the pinned case are always larger than those for the free sliding case, because the interface shape is constrained more by the pinned condition than the natural free sliding condition, as is well known [45]. To be more precise, the free sliding boundary condition is compatible with the no-penetration condition at the container sidewall, and is therefore naturally satisfied, whereas the pinned boundary condition is incompatible and, accordingly, the interface shape must adapt itself to satisfy both conditions, making the pinned condition more "constrained." Lastly, we contrast the instability tongues for the two liquid heights considered here: $H = 7$ mm [Fig. 5(a)] and $H = 22$ mm [Fig. 5(b)], showing that (i) the threshold acceleration increases with decreasing liquid height for both pinned and free sliding edge conditions, and (ii) the natural frequencies increase with increasing liquid height. We attribute the former to the smaller inertial force associated with a relatively smaller liquid mass for fixed acceleration, whereas the latter is a well-known property of capillary-gravity waves [53].

Viscous effects are systematically investigated using glycerol/water mixtures, as shown in Fig. 6, which is a plot of the instability tongues in the (f_d, A) space for $H = 22$ mm. Here the contact-line is pinned for all experiments. The full frequency scan is shown in Fig. 6(a) with the isolated (1,2) mode given in Fig. 6(b). For a given mode (n, ℓ), the instability tongue shifts to (i) lower frequency and (ii) higher acceleration with increasing viscosity, as clearly illustrated in Fig. 6(b). Here a larger acceleration is required to overcome the increased viscous dissipation, as could be expected. The natural frequency shift can be understood from the underdamped oscillations of the simple damped

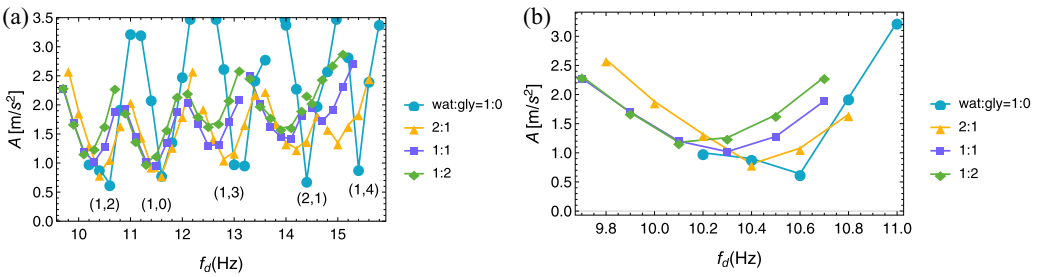

FIG. 6. Acceleration A against driving frequency f_d for glycerol/water mixtures with height $H = 22$ mm and pinned contact-line illustrating (a) the full frequency scan and (b) only the (1,2) mode.

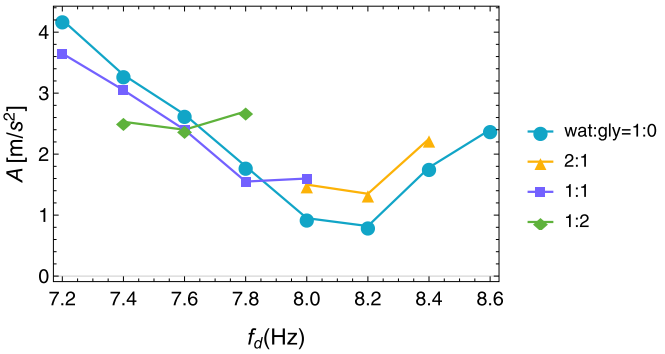

FIG. 7. Acceleration A against driving frequency f_d for glycerol/water mixtures with height $H = 7$ mm and pinned contact-line for the (1,2) mode.

oscillator $\ddot{x} + 2\beta\dot{x} + \omega_0^2 x = 0$ by associating the damping constant β with the viscosity and looking at the oscillation frequency $\omega = \sqrt{\omega_0^2 - \beta^2}$. Here increasing β (equivalently, viscosity) leads to a decrease in oscillation frequency, consistent with our experimental observations. Figure 7 is a plot of the instability tongue for the (1,2) mode for $H = 7$ mm, which shows an increased acceleration threshold and natural frequency shift to lower values relative to the $H = 22$ mm case [cf. Fig. 6(b)]. This observation is consistent with those discussed above regarding the role of liquid height H.

IV. THEORETICAL MODEL

We generalize the model presented by Shao *et al.* [54] to asymmetric surface waves on a viscoelastic material in a cylindrical container of radius R and height H. Here we assume the interface is flat, endowed with surface tension σ, and given a small disturbance ξ that induces an interfacially driven flow defined by velocity $\boldsymbol{v}$ and pressure p fields. Viscous potential flow (VPF) is applied, whereby the bulk dissipation from viscosity is approximated from the irrotational flow field $\boldsymbol{v} = \nabla\Phi$, with Φ the velocity potential [53,55]. Two different contact-line conditions are considered: (i) freely sliding and (ii) pinned, as shown in Fig. 2.

A. Hydrodynamic field equations

The fluid is assumed to be incompressible and the flow irrotational, thus the velocity potential Φ satisfies Laplace's equation

$$\nabla^2\Phi = 0, \tag{1}$$

as required by continuity. The velocity potential satisfies the no-penetration condition

$$\left.\frac{\partial\Phi}{\partial r}\right|_{r=R} = 0, \quad \left.\frac{\partial\Phi}{\partial z}\right|_{z=0} = 0 \tag{2}$$

at the walls of the cylindrical container, and a kinematic condition

$$\frac{\partial\Phi}{\partial z} = \frac{\partial\xi}{\partial t} \tag{3}$$

on the free surface $z = H$, which relates the normal velocity to the perturbation amplitude there. Note that the no-slip condition cannot be satisfied for VPF. The pressure field in the fluid is given by the linearized Bernoulli equation

$$p = -\rho\frac{\partial\Phi}{\partial t} - \rho g\xi, \tag{4}$$

where ρ is the fluid density and g is the gravitational constant. The pressure at the free surface is governed by the linearized Young-Laplace equation

$$p - 2\mu\frac{\partial^2\Phi}{\partial z^2} = -\sigma\left(\frac{\partial^2\xi}{\partial r^2} + \frac{1}{r}\frac{\partial\xi}{\partial r} + \frac{1}{r^2}\frac{\partial^2\xi}{\partial\theta^2}\right), \tag{5}$$

valid for small disturbances $|\xi| \ll 1$ with μ the viscosity. Lastly, volume conservation is enforced by the integral condition

$$\int_0^{2\pi}\int_0^R r\xi(r,\theta)dr\,d\theta = 0. \tag{6}$$

Equations (1)–(6) are the linearized disturbance equations, which are augmented with a contact-line condition at the container sidewall. The first condition we consider is that of a freely sliding contact-line in which the contact-line is free to move with a prescribed angle (90° in our case),

$$\xi'|_{r=R} = 0. \tag{7}$$

The second condition is that of a pinned or immobile contact-line, which requires zero displacement there,

$$\xi|_{r=R} = 0. \tag{8}$$

This choice of contact-line condition affects the predicted frequencies and is our focus so as to relate to the corresponding experimental results described above.

B. Normal modes

Dimensionless variables are introduced,

$$\bar{r} = r/R, \quad \bar{z} = z/R, \quad \bar{\xi} = \xi/R, \quad \bar{t} = t\sqrt{\frac{\sigma}{\varrho R^3}}, \quad \bar{\Phi} = \Phi\sqrt{\frac{\rho}{\sigma R}}, \quad \bar{p} = p\left(\frac{R}{\sigma}\right). \tag{9}$$

Lengths are scaled by the radius of the cylinder R, time with the capillary timescale $\sqrt{\rho R^3/\sigma}$, and pressure with the capillary pressure σ/R. Viscoelasticity enters the governing equations through the complex viscosity $\mu \to \mu + G/i\omega$, with G the shear modulus and ω the frequency [56]. For simplicity, we assume that both μ and G are constant, which is a good approximation for soft polymeric gels [57].

Normal modes,

$$\Phi(\boldsymbol{x},t) = \phi(r,z)e^{i\omega t}e^{i\ell\theta}, \quad \xi(r,\theta,t) = y(r)e^{i\omega t}e^{i\ell\theta}, \tag{10}$$

are then applied with the scalings (9) to the domain equations to yield

$$\frac{1}{r}\frac{\partial}{\partial r}\left(r\frac{\partial\phi}{\partial r}\right) - \frac{\ell^2}{r^2}\phi + \frac{\partial^2\phi}{\partial z^2} = 0, \quad p = -i\lambda\phi - \mathrm{Bo}y, \tag{11}$$

with corresponding boundary conditions

$$\left.\frac{\partial\phi}{\partial r}\right|_{r=1} = 0, \quad \left.\frac{\partial\phi}{\partial z}\right|_{z=0} = 0, \quad \left.\frac{\partial\phi}{\partial z}\right|_{z=h} = i\lambda y,$$
$$p - 2\left(\mathrm{Oh} + \frac{\mathrm{Ec}}{i\lambda}\right)\left.\frac{\partial^2\phi}{\partial z^2}\right|_{z=h} = -\left(\frac{\partial^2 y}{\partial r^2} + \frac{1}{r}\frac{\partial y}{\partial r} - \frac{\ell^2}{r^2}y\right). \tag{12}$$

Here $\lambda \equiv \omega\sqrt{\rho R^3/\sigma}$ is the scaled frequency, $h = H/R$ is the cylinder aspect ratio, $\mathrm{Bo} \equiv \rho g R^2/\sigma$ is the Bond number, $\mathrm{Oh} \equiv \mu/\sqrt{\rho R\sigma}$ is the Ohnesorge number, and $\mathrm{Ec} \equiv GR/\sigma$ is the elastocapillary number. The volume conservation constraint (6) is naturally satisfied for $\ell \neq 0$, but for $\ell = 0$ it

requires

$$\int_0^1 r y(r) dr = 0. \tag{13}$$

C. Integrodifferential equation

The solution for the velocity potential is given by

$$\phi(r,z) = i\lambda \sum_{n=1}^{\infty} \frac{1}{k_{n\ell}} \frac{\cosh(k_{n\ell} z)}{\sinh(k_{n\ell} h)} \frac{\langle y, J_\ell(k_{n\ell} r)\rangle}{\langle J_\ell(k_{n\ell} r), J_\ell(k_{n\ell} r)\rangle} J_\ell(k_{n\ell} r), \tag{14}$$

where $k_{n\ell}$ is the nth zero of $J'_\ell(k)$, as required to satisfy the no-penetration condition at the lateral side wall ($r = 1$), with J_ℓ the Bessel function. The inner product is defined as

$$\langle f(r), g(r)\rangle = \int_0^1 r f(r) g(r) dr. \tag{15}$$

Substituting (14) into the governing equations and simplifying yields an integrodifferential equation for the disturbance y,

$$\begin{aligned}
&\lambda^2 \sum_{n=1}^{\infty} \frac{\coth(k_{n\ell} h)}{k_n} \frac{\langle y, J_\ell(k_{n\ell} r)\rangle}{\langle J_\ell(k_{n\ell} r), J_\ell(k_{n\ell} r)\rangle} J_\ell(k_{n\ell} r) \\
&\quad - 2i\lambda\,\mathrm{Oh} \sum_{n=1}^{\infty} k_{n\ell} \coth(k_{n\ell} h) \frac{\langle y, J_\ell(k_{n\ell} r)\rangle}{\langle J_\ell(k_{n\ell} r), J_\ell(k_{n\ell} r)\rangle} J_\ell(k_{n\ell} r) \\
&\quad - 2\,\mathrm{Ec} \sum_{n=1}^{\infty} k_{n\ell} \coth(k_{n\ell} h) \frac{\langle y, J_\ell(k_{n\ell} r)\rangle}{\langle J_\ell(k_{n\ell} r), J_\ell(k_{n\ell} r)\rangle} J_\ell(k_{n\ell} r) - \mathrm{Bo}\, y + \left[\frac{d^2 y}{dr^2} + \frac{1}{r}\frac{dy}{dr} - \frac{\ell^2}{r^2} y\right] = 0,
\end{aligned} \tag{16}$$

which is augmented by either the (i) freely sliding or (ii) pinned contact-line condition.

D. Operator formalism

It will be useful to recast (16) as an operator equation

$$\lambda^2 M[y] + \lambda D[y; \mathrm{Oh}] + K[y; \mathrm{Bo}, \mathrm{Ec}] = 0, \tag{17}$$

with

$$M[y] \equiv \sum_{n=1}^{\infty} \frac{1}{k_{n\ell}} \coth(k_{n\ell} h) \frac{\langle y, J_\ell(k_{n\ell} r)\rangle}{\langle J_\ell(k_{n\ell} r), J_\ell(k_{n\ell} r)\rangle} J_\ell(k_{n\ell} r) \tag{18}$$

an integral operator representative of the fluid inertia,

$$D[y; \mathrm{Oh}] \equiv -2i\,\mathrm{Oh} \sum_{n=1}^{\infty} k_{n\ell} \coth(k_{n\ell} h) \frac{\langle y, J_\ell(k_{n\ell} r)\rangle}{\langle J_\ell(k_{n\ell} r), J_\ell(k_{n\ell} r)\rangle} J_\ell(k_{n\ell} r) \tag{19}$$

the dissipation operator, and

$$K[y;\mathrm{Bo},\mathrm{Ec}] \equiv -2\,\mathrm{Ec}\sum_{n=1}^{\infty} k_{n\ell}\coth(k_{n\ell}h)\frac{\langle y, J_\ell(k_{n\ell}r)\rangle}{\langle J_\ell(k_{n\ell}r), J_\ell(k_{n\ell}r)\rangle}J_\ell(k_{n\ell}r) - \mathrm{Bo}\,y + \left[\frac{d^2}{dr^2}+\frac{1}{r}\frac{d}{dr}-\frac{\ell^2}{r^2}\right]y \tag{20}$$

a differential operator representative of the restorative forces of surface tension, elasticity, and gravity.

E. Dispersion relationship for a freely sliding contact-line

The function $y = J_\ell(k_{n\ell}r)$ is a solution to (17) with a freely sliding contact-line (7), and it gives the dispersion relationship

$$\lambda_{n\ell} = i\,\mathrm{Oh}k_{n\ell}^2 \pm \sqrt{\left(\mathrm{Bo}k_{n\ell}+k_{n\ell}^3\right)\tanh\left(k_{n\ell}h\right)+2k_{n\ell}^2\mathrm{Ec}-\mathrm{Oh}^2k_{n\ell}^4}, \tag{21}$$

where Re[λ] is the frequency and Im[λ] is the decay rate of oscillation. The freely sliding condition is sometimes referred to as the natural boundary condition associated with the no-penetration condition at the sidewall. We note that the integral constraint (13) for $\ell = 0$ is naturally satisfied for this solution. This is easily seen by applying a Bessel function identity to $\int_0^1 rJ_0(kr)dr = -J_0'(k)/k^2$ and realizing that k_{n0} was chosen such that $J_0'(k) = 0$, which gives the desired result $\int_0^1 rJ_0(k_{n0}r)dr = 0$.

F. Solution method for the pinned contact-line

In contrast to the freely sliding contact-line, the pinned contact-line condition (8) is incompatible with the no-penetration condition, which makes it difficult to satisfy this condition. We use a Rayleigh-Ritz method to construct an approximate solution to the eigenvalue problem (17) by building the pinned contact-line condition and volume conservation condition (13) into the function space over which the minimization is done [58]. This is a variational approach, and it has been applied previously to constrained drops by Bostwick and Steen [37,59,60].

We begin by constructing a constrained function space that is spanned by a set of functions that satisfy the pinned edge condition,

$$S_{n\ell}(r) = J_\ell(k_{n\ell}r) - \frac{J_\ell(k_{n\ell})}{J_\ell(k_{1\ell})}J_\ell(k_{1\ell}r), \quad n = 2, 3, \ldots, N. \tag{22}$$

Note that the summation starts at $n = 2$. We then apply a Gram-Schmidt procedure to the functions $S_{n\ell}$ in order to generate a set of orthonormal basis functions $V_i(r)$, with $\int_0^1 rV_i(r)V_j(r)dr = \delta_{ij}$, where δ_{ij} is the Kronecker delta function. These functions span the constrained function space, and

TABLE II. Theoretical natural frequency (Hz) and % difference (in parentheses) from experiment for Triton/water mixtures.

Mode	(1,2)	(1,0)	(1,3)	(2,1)
$H = 22$ mm				
Sliding	4.63(3.7%)	5.30(1.9%)	5.59(3.7%)	6.43(1.1%)
Pinned	5.11(2.2%)	5.61(0.2%)	6.23(2.1%)	6.83(0.4%)
$H = 7$ mm				
Sliding	3.49(0.3%)	4.29(2.1%)	4.66(0.9%)	5.72(2.1%)
Pinned	3.89(0.1%)	4.57(1.6%)	5.25(2.9%)	6.10(1.6%)

TABLE III. Theoretical natural frequency (Hz) and % difference (in parentheses) from experiment for water/glycerol (w:g) mixtures with $H = 22$ mm.

Mode	(1,2)	(1,0)	(1,3)	(2,1)	(1.4)
w:g=1:0	5.33(0.6%)	5.82(0.4%)	6.58(0.3%)	7.21(0.1%)	7.72(0.2%)
2:1	5.27(1.3%)	5.76(0.7%)	6.48(1.2%)	7.09(0.1%)	7.57(0.9%)
1:1	5.23(1.6%)	5.73(0.4%)	6.43(2.8%)	7.04(0.2%)	7.49(1.9%)
1:2	5.21(3.1%)	5.71(1.0%)	6.39(2.2%)	6.99(0.6%)	7.43(2.5%)

we can write y as

$$y(r) = \sum_{i=1}^{\infty} c_i V_i(r). \tag{23}$$

This solution series is then applied to the operator equation (17), and inner products are taken to yield the matrix equation

$$(\lambda^2 \mathbf{M} + \lambda \mathbf{D} + \mathbf{K})\mathbf{c} = 0, \tag{24}$$

with matrices $\mathbf{M}$, $\mathbf{D}$, and $\mathbf{K}$ defined as

$$\mathbf{M} = \langle M[V_i], V_j \rangle, \quad \mathbf{D} = \langle D[V_i], V_j \rangle, \quad \mathbf{K} = \langle K[V_i], V_j \rangle, \tag{25}$$

and $\boldsymbol{c}$ is the coefficient vector.

V. COMPARISON BETWEEN THEORY AND EXPERIMENT

For the free sliding contact-line, the oscillation frequencies are readily computed from (21) and it is straightforward to interpret how material properties affect the frequency from this equation. For an inviscid material $\mathrm{Oh} = 0$, the imaginary part of the frequency is zero, i.e., zero decay rate; the real part increases with wave number k, aspect ratio h, Bond number Bo, and elastocapillary number Ec. These observations are qualitatively consistent with our experimental observations on the role of liquid height H (equivalently, h) and elasticity G (equivalently, Ec). In contrast, for a viscous material $\mathrm{Oh} \neq 0$ there is decay rate (imaginary part) associated with frequency, and inspection of (21) reveals that the oscillation frequency (real part) decreases with increasing Oh. This is also consistent with our experiments that investigate the role of viscosity μ (equivalently, Oh).

These qualitative trends with respect to the dimensionless parameters also hold for the pinned contact-line condition. However, the numerical computation of the frequencies from the eigenvalue problem (24) is more involved, and we use the MATLAB function polyeig to compute the eigenvalue/vector pairs $(\lambda, \mathbf{c})$. Here we use $N = 30$ terms in the solution series, and this produces a relative eigenvalue convergence of 0.01%. Each eigenvalue $\lambda_{n,\ell}$ and eigenvector $\boldsymbol{c}_{n,\ell}$ pair can be distinguished by the mode number pair (n, ℓ), where n and ℓ are the radial and azimuthal mode

TABLE IV. Theoretical natural frequency (Hz) and % difference (in parentheses) from experiment for water/glycerol (w:g) mixtures with $H = 7$ mm.

Mode	(1,2)	(1,0)	(1,3)	(2,1)	(1.4)
w:g=1:0	4.07(0.8%)	4.75(1.1%)	5.55(0.9%)	6.43(0.4%)	6.93(0.5%)
2:1	4.02(1.9%)	4.70(0.0%)	5.47(0.5%)	6.34(1.0%)	6.81(1.3%)
1:1	3.99(2.4%)	4.67(0.6%)	5.42(0.4%)	6.28(0.3%)	6.74(0.6%)
1:2	3.98(4.6%)	4.66(1.2%)	5.40(3.7%)	6.25(0.9%)	6.79(1.5%)

TABLE V. Comparison of natural frequency (Hz) between experiment and theory for the (1,2) mode on agarose gel, taken from Shao *et al.* [26].

G (Pa)	Experiment	Theory	% difference
0 (water)	5.3	5.33	0.5%
0.4	5.1	5.35	4.8%
0.8	5.2	5.37	3.3%
3.1	5.3	5.50	3.7%
3.5	5.5	5.52	0.4%
4.0	5.8	5.55	4.4%
10.1	6.0	5.87	1.3%
12.2	6.1	5.98	2.0%

numbers, respectively. These can be compared directly with experiment in which we have identified the modal structure using a 2D cross-correlation, as described in an earlier section.

Given that our model predicts the natural frequency of oscillation, as it depends upon Bo, Oh, Ec, h and the edge conditions, pinned or free-sliding, we are interested in comparing these predictions with the observed natural frequency in experiment. We note that our experiments were performed for intermediate values of the Bond number Bo, such that both surface tension and gravitational forces are important, with the relative importance depending upon the mode number pair (equivalently, wavelength), as shown in our prior work for an inviscid fluid (Ref. [46], Fig. 13b). Recall that for Faraday waves the observed oscillation frequency is half the driving frequency, and here we report the surface wave frequency in our comparisons. Here the maximum potential error in natural frequency is bounded by the experimental frequency interval or 0.1 Hz (equivalently, 0.2 Hz in driving frequency). The agreement between theory and experiment is generally very good, with a maximum error of approximately 5.2% and the majority of errors less than 1%. This suggests our model accurately captures the physics of oscillations of surface waves in viscoelastic materials over a range of mode numbers, material parameters, and edge conditions.

Table II shows the comparison for the Triton/water mixtures, as it depends upon the edge conditions, i.e., sliding or pinned (cf. Fig. 5). Note that the pinned frequency is always greater than the sliding frequency, because the pinned condition is more constrained than the natural free sliding condition, resulting in a higher frequency. Here the prediction is generally better for the pinned condition than the free sliding condition. For glycerol/water mixtures, Tables III and IVshow the comparison for liquid heights of $H = 22$ and 7 mm, respectively, and the agreement is very good, although we note that error tends to increase with viscosity (i.e., glycerol concentration). For the agarose gels, Tables V and VI give the comparison for the (1,2) and (1,3) modes observed in Ref. [26], respectively, and the agreement is also very good. Here the natural frequency increases with increasing shear modulus, consistent with the role of elasticity as a restorative force that resists

TABLE VI. Comparison of natural frequency (Hz) between experiment and theory for the (1,3) mode on agarose gel, taken from Shao *et al.* [26].

G (Pa)	Experiment	Theory	% difference
0 (water)	6.5	6.58	1.2%
0.4	6.4	6.61	3.2%
1.2	6.4	6.68	4.2%
3.9	6.6	6.90	5.2%

the material inertia. Relative to water ($G = 0$ Pa), there is a shift to lower frequencies for a small range of $G < 3.1$ Pa, and we attribute this to a small, but non-negligible, loss modulus G'' that manifests itself as a "solid" viscosity with commensurate effects on the natural frequency. There does not appear to be a trend with the error for the agarose gels.

VI. CONCLUDING REMARKS

We have studied the pattern formation of Faraday waves in a cylindrical container filled with a viscoelastic material. Our focus was on how (i) edge effects and (ii) fluid depth affect the shape of the instability tongue. Experiments were performed using a shaker system and laser light detection method to obtain the instability tongues for Faraday waves. Long exposure time white light imaging was used to determine the surface wave structure, which is defined by the mode number pair (n, ℓ) as determined by 2D cross-correlation analysis. Triton/water mixtures were used to investigate edge (contact-line) effects, glycerol/water mixtures to study viscous effects, and agarose gels to study elastic effects. Our experiments compare favorably with our theoretical model. We derive a closed-form expression for the dispersion relationship for free-sliding edge conditions [Eq. (21)], and we use a Rayleigh-Ritz variational procedure for the pinned edge condition to compute the natural frequency for a viscoelastic material. Theory and experiment show that the pinned condition always generates larger frequencies than the free sliding condition, and this is related to the degree of constraint the boundary condition enforces on the interface shape. The quantitative agreement between experiment and theory over a large range of parameters suggests that our model captures the essential physics. This is despite the fact that our model does not include effects due to the viscous boundary layer [61,62], the static contact angle [63], or dynamic contact-line effects [64,65].

Future extensions to this work could include investigations of viscoelastic materials with a more complex frequency-dependent rheology that exhibit, e.g., shear-thinning (xanthan gum), shear-thickening (cornstarch/water mixtures), or yield stress (carbopol) behavior. We purposefully chose materials with frequency-independent properties over the range of experimental frequencies investigated in order to clearly isolate the role of viscosity and elasticity. More complicated dynamics can be expected for more complex materials, particularly those that exhibit a crossover (solidlike to fluidlike behavior) frequency in the range of experimental driving frequencies.

Lastly, we note that we did not observe any modal reordering, like that observed in sessile drops [66–68] for varying contact angle, with respect to any of the material parameters in our experiments. This may be because we were careful to ensure a flat interface (contact angle $\alpha = 90^\circ$) during experiment. Our experiments were conducted in tanks with a relatively large radius, with an equivalently large Bond number, and any geometric wetting effect would be localized at the meniscus near the container wall with the interface remaining largely flat along the container diameter. However, the presence of a meniscus is known to induce harmonic edge waves that could contaminate any pure investigation of Faraday waves [36]. We note that we have observed modal mixing of harmonic edge waves and subharmonic Faraday waves for the same driving frequency in water [46]. Much smaller tanks would be needed to investigate geometric contact angle effects and any potential modal reordering.

ACKNOWLEDGMENTS

J.B.B. acknowledges support from NSF Grant No. CMMI-1935590.

[1] M. Faraday, XVII. On a peculiar class of acoustical figures; and on certain forms assumed by groups of particles upon vibrating elastic surfaces, Philos. Trans. R. Soc. London 299 (1831).
[2] J. Miles and D. Henderson, Parametrically forced surface waves, Annu. Rev. Fluid Mech. **22**, 143 (1990).
[3] M. Perlin and W. W. Schultz, Capillary effects on surface waves, Annu. Rev. Fluid Mech. **32**, 241 (2000).

[4] A. James, B. Vukasinovic, M. K. Smith, and A. Glezer, Vibration-induced drop atomization and bursting, J. Fluid Mech. **476**, 1 (2003).
[5] B. Vukasinovic, M. K. Smith, and A. Glezer, Dynamics of a sessile drop in forced vibration, J. Fluid Mech. **587**, 395 (2007).
[6] C. S. Tsai, R. W. Mao, S. K. Lin, Y. Zhu, and S. C. Tsai, Faraday instability-based micro droplet ejection for inhalation drug delivery, Technology **02**, 75 (2014).
[7] P. H. Wright and J. R. Saylor, Patterning of particulate films using Faraday waves, Rev. Sci. Instrum. **74**, 4063 (2003).
[8] J. R. Saylor and A. L. Kinard, Simulation of particle deposition beneath Faraday waves in thin liquid films, Phys. Fluids **17**, 047106 (2005).
[9] A. Briard, L. Gostiaux, and B.-J. Gréa, The turbulent Faraday instability in miscible fluids, J. Fluid Mech. **883**, A57(2020).
[10] J. R. Saylor and R. A. Handler, Gas transport across an air/water interface populated with capillary waves, Phys. Fluids **9**, 2529 (1997).
[11] J. R. Saylor and R. A. Handler, Capillary wave gas exchange in the presence of surfactants, Exp. Fluids **27**, 332 (1999).
[12] J. R. Saylor, The rôle of capillary waves in oceanic air/water gas exchange, Tellus B: Chem. Phys. Meteorol. **51** , 616 (1999).
[13] P. Chen, S. Güven, O. B. Usta, M. L. Yarmush, and U. Demirci, Biotunable acoustic node assembly of organoids, Adv. Healthcare Mater. **4**, 1937 (2015).
[14] S. Guven, P. Chen, F. Inci, S. Tasoglu, B. Erkmen, and U. Demirci, Multiscale assembly for tissue engineering and regenerative medicine, Trends Biotechnol. **33**, 269 (2015).
[15] S. V. Murphy and A. Atala, 3D bioprinting of tissues and organs, Nat. Biotechnol. **32**, 773 (2014).
[16] R. Fan, M. Piou, E. Darling, D. Cormier, J. Sun, and J. Wan, Bio-printing cell-laden matrigel–agarose constructs, J. Biomater. Appl. **31**, 684 (2016).
[17] B. Christiansen, P. Alstrom, and M. T. Levinsen, Ordered Capillary-Wave States: Quasicrystals, Hexagons, and Radial Waves, Phys. Rev. Lett. **68**, 2157 (1992).
[18] K. Kumar and K. M. S. Bajaj, Competing patterns in the Faraday experiment, Phys. Rev. E **52**, R4606 (1995).
[19] W. S. Edwards and S. Fauve, Patterns and quasi-patterns in the Faraday experiment, J. Fluid Mech. **278**, 123 (1994).
[20] T. B. Benjamin and F. J. Ursell, The stability of the plane free surface of a liquid in vertical periodic motion, Proc. R. Soc. London, Ser. A **225**, 505 (1954).
[21] K. Kumar, Linear theory of faraday instability in viscous liquids, Proc. R. Soc. London, Ser. A **452**, 1113 (1996).
[22] H. W. Müller, H. Wittmer, C. Wagner, J. Albers, and K. Knorr, Analytic Stability Theory for Faraday Waves and the Observation of the Harmonic Surface Response, Phys. Rev. Lett. **78**, 2357 (1997).
[23] S. Kumar, Parametrically driven surface waves in viscoelastic liquids, Phys. Fluids **11**, 1970 (1999).
[24] C. Wagner, H. W. Müller, and K. Knorr, Faraday Waves on a Viscoelastic Liquid, Phys. Rev. Lett. **83**, 308 (1999).
[25] D. Joseph, T. Funada, and J. Wang, *Potential Flows of Viscous and Viscoelastic Liquids*, Cambridge Aerospace Series (Cambridge University Press, Cambridge, 2007)
[26] X. Shao, G. Bevilacqua, P. Ciarletta, J. R. Saylor, and J. B. Bostwick, Experimental observation of Faraday waves in soft gels, Phys. Rev. E **102**, 060602(R) (2020).
[27] T. G. Mezger, *The Rheology Handbook: For Users of Rotational and Oscillatory Rheometers* (Vincentz Network, Hannover, 2006).
[28] R. W. Style, A. Jagota, C.-Y. Hui, and E. R. Dufresne, Elastocapillarity: Surface tension and the mechanics of soft solids, Annu. Rev. Condens. Matter Phys. **8**, 99 (2017).
[29] J. Bico, É. Reyssat, and B. Roman, Elastocapillarity: When surface tension deforms elastic solids, Annu. Rev. Fluid Mech. **50**, 629 (2018).
[30] S. Douady and S. Fauve, Pattern selection in Faraday instability, Europhys. Lett. **6**, 221 (1988).
[31] S. Douady, Experimental study of the Faraday instability, J. Fluid Mech. **221**, 383 (1990).

[32] D. M. Henderson and J. W. Miles, Single-mode Faraday waves in small cylinders, J. Fluid Mech. **213**, 95 (1990).
[33] D. M. Henderson and J. W. Miles, Faraday waves in 2:1 internal resonance, J. Fluid Mech. **222**, 449 (1991).
[34] W. Batson, F. Zoueshtiagh, and R. Narayanan, The Faraday threshold in small cylinders and the sidewall non-ideality, J. Fluid Mech. **729**, 496 (2013).
[35] K. Ward, F. Zoueshtiagh, and R. Narayanan, Faraday instability in double-interface fluid layers, Phys. Rev. Fluids **4**, 043903 (2019).
[36] X. Shao, C. T. Gabbard, J. B. Bostwick, and J. R. Saylor, On the role of meniscus geometry in capillary wave generation, Exp. Fluids **62**, 59 (2021).
[37] J. B. Bostwick and P. H. Steen, Capillary oscillations of a constrained liquid drop, Phys. Fluids **21**, 032108 (2009).
[38] J. B. Bostwick and P. H. Steen, Static rivulet instabilities: varicose and sinuous modes, J. Fluid Mech. **837**, 819 (2018).
[39] T. B. Benjamin and J. C. Scott, Gravity-capillary waves with edge constraints, J. Fluid Mech. **92**, 241 (1979).
[40] J. Graham-Eagle, A new method for calculating eigenvalues with applications to gravity-capillary waves with edge constraints, in *Mathematical Proceedings of the Cambridge Philosophical Society* (Cambridge University Press, Cambridge, 1983), Vol. 94, pp. 553–564.
[41] A. Prosperetti, Linear oscillations of constrained drops, bubbles, and plane liquid surfaces, Phys. Fluids **24**, 032109 (2012).
[42] S. H. Davis, Moving contact lines and rivulet instabilities. Part 1. The static rivulet, J. Fluid Mech. **98**, 225 (1980).
[43] D. V. Lyubimov, T. P. Lyubimova, and S. V. Shklyaev, Behavior of a drop on an oscillating solid plate, Phys. Fluids **18**, 012101 (2006).
[44] J. B. Bostwick and P. H. Steen, Response of driven sessile drops with contact-line dissipation, Soft Matter **12**, 8919 (2016).
[45] J. B. Bostwick and P. H. Steen, Stability of constrained capillary surfaces, Annu. Rev. Fluid Mech. **47**, 539 (2015).
[46] X. Shao, P. Wilson, J. R. Saylor, and J. B. Bostwick, Surface wave pattern formation in a cylindrical container, J. Fluid Mech. **915**, A19 (2021).
[47] K. Takamura, H. Fischer, and N. R. Morrow, Physical properties of aqueous glycerol solutions, J. Pet. Sci. Eng. **98–99**, 50 (2012).
[48] Q. Jiang, Y. C. Chiew, and J. E. Valentini, Damping of cylindrical propagating capillary waves on monolayer-covered surfaces, Langmuir **8**, 2747 (1992).
[49] J. R. Saylor, Internal reflection beneath capillary water waves: A method for measuring wave slope, Appl. Opt. **36**, 1121 (1997).
[50] A. V. Kityk, J. Embs, V. V. Mekhonoshin, and C. Wagner, Spatiotemporal characterization of interfacial Faraday waves by means of a light absorption technique, Phys. Rev. E **72**, 036209 (2005).
[51] F. Moisy, M. Rabaud, and K. Salsac, A synthetic Schlieren method for the measurement of the topography of a liquid surface, Exp. Fluids **46**, 1021 (2009).
[52] S. L. Strickland, M. Shearer, and K. E. Daniels, Spatiotemporal measurement of surfactant distribution on gravity-capillary waves, J. Fluid Mech. **777**, 523 (2015).
[53] H. Lamb, *Hydrodynamics* (Cambridge University Press, Cambridge, 1932).
[54] X. Shao, P. Wilson, J. B. Bostwick, and J. R. Saylor, Viscoelastic effects in circular edge waves, J. Fluid Mech. **919**, A18 (2021).
[55] J. C. Padrino, T. Funada, and D. D. Joseph, Purely irrotational theories for the viscous effects on the oscillations of drops and bubbles, Int. J. Multiphase Flow **34**, 61 (2008).
[56] J. L. Harden, H. Pleiner, and P. A. Pincus, Hydrodynamic surface modes on concentrated polymer solutions and gels, J. Chem. Phys. **94**, 5208 (1991).
[57] M. Tokita and K. Hikichi, Mechanical studies of sol-gel transition: Universal behavior of elastic modulus, Phys. Rev. A **35**, 4329 (1987).

[58] L. A. Segel, *Mathematics Applied to Continuum Mechanics* (Dover, New York, 1987).
[59] J. B. Bostwick and P. H. Steen, Coupled oscillations of deformable spherical-cap droplets. Part 1. Inviscid motions, J. Fluid Mech. **714**, 312 (2013).
[60] J. B. Bostwick and P. H. Steen, Coupled oscillations of deformable spherical-cap droplets. Part 2. Viscous motions, J. Fluid Mech. **714**, 336 (2013).
[61] D. M. Henderson and J. W. Miles, Surface-wave damping in a circular cylinder with a fixed contact line, J. Fluid Mech. **275**, 285 (1994).
[62] J. A. Nicolás, The viscous damping of capillary-gravity waves in a brimful circular cylinder, Phys. Fluids **14**, 1910 (2002).
[63] J. A. Nicolás, Effects of static contact angles on inviscid gravity-capillary waves, Phys. Fluids **17**, 022101 (2005).
[64] R. Kidambi, Capillary damping of inviscid surface waves in a circular cylinder, J. Fluid Mech. **627**, 323 (2009).
[65] R. Kidambi, Meniscus effects on the frequency and damping of capillary-gravity waves in a brimful circular cylinder, Wave Motion **46**, 144 (2009).
[66] J. B. Bostwick and P. H. Steen, Dynamics of sessile drops. Part 1. Inviscid theory, J. Fluid Mech. **760**, 5 (2014).
[67] C.-T. Chang, J. B. Bostwick, S. Daniel, and P. H. Steen, Dynamics of sessile drops. Part 2. Experiment, J. Fluid Mech. **768**, 442 (2015).
[68] P. H. Steen, C.-T. Chang, and J. B. Bostwick, Droplet motions fill a periodic table, Proc. Natl. Acad. Sci. USA **116**, 4849 (2019).